ELSEVIER

Multiscale boundary conditions in crystalline solids: Theory and application to nanoindentation

E.G. Karpov [a,*], H. Yu [a], H.S. Park [b], Wing Kam Liu [a], Q. Jane Wang [a], D. Qian [c]

[a] *Department of Mechanical Engineering, Northwestern University, 2145 Sheridan Road, Evanston, IL 60208, United States*
[b] *Department of Civil and Environmental Engineering, Vanderbilt University, Nashville, TN 37235, United States*
[c] *Department of Mechanical, Industrial and Nuclear Engineering, University of Cincinnati, P.O. Box 210072, Cincinnati, OH 45221, United States*

Abstract

This paper presents a systematic approach to treating the interfaces between the localized (fine grain) and peripheral (coarse grain) domains in atomic scale simulations of crystalline solids. Based on Fourier analysis of regular lattices structures, this approach allows elimination of unnecessary atomic degrees of freedom over the coarse grain, without involving an explicit continuum model for the latter. The mathematical formulation involves compact convolution operators that relate displacements of the interface atoms and the adjacent atoms on the coarse grain. These operators are defined by geometry of the lattice structure, and interatomic potentials. Application and performance are illustrated on quasistatic nanoindentation simulations with a crystalline gold substrate. Complete atomistic resolution on the coarse grain is alternatively employed to give the benchmark solutions. The results are found to match well for the multiscale and the full atomistic simulations.
© 2005 Elsevier Ltd. All rights reserved.

Keywords: Boundary conditions; Multiscale simulation; Molecular dynamics; Crystal structure; Nanoindentation

1. Introduction

Over the past few decades, continuum methods have dominated materials modeling research. This approach of predicting material deformation and failure by implicitly averaging atomic scale mechanics and defect evolution over time and space, however, is valid only for sufficiently large systems that include a substantial number of inhomogeneities. As a result, numerous experimental observations of material behavior cannot be readily explained within the continuum mechanics framework: dislocation patterns in fatigue and creep, surface roughening and crack nucleation in fatigue, the inherent inhomogeneity of plastic deformation, the statistical nature of brittle failure, plastic flow localization in shear bands, and the effects of size, geometry,

---
* Corresponding author. Tel.: +1 847 491 3915.
  E-mail address: ekarpov@northwestern.edu (E.G. Karpov).

and stress state on yield properties. Thus, there is a considerable effort to find fundamental descriptions of strength and failure properties of nanoscale materials, taking into account their atomic structures. The use of molecular dynamics/quasistatic atomistic simulations has provided useful information on material behavior at the nanoscale. However, typical atomistic simulations are still restricted to very small systems consisting of several million atoms or less and timescales on the order of picoseconds. Thus, even for nanoscale structures and materials, atomistic modeling would be computationally prohibitive. The limitations of atomistic simulations and continuum mechanics, along with practical needs arising from the heterogeneous nature of engineering materials, have motivated the research on multiscale simulation methods that bridge atomistic simulations and continuum modeling; examples include the works by Curtin and Miller (2003), Liu et al. (2004), Shilkrot et al. (2004), Broughton et al. (1999), Abraham et al. (1998), Rudd and Broughton (1998, 2000), Tadmor et al. (1996), Shenoy et al. (1998), Ortiz et al. (2001), Deymier and Vasseur (2002), Wagner and Liu (2003) and Park et al. (2005b,c). In order to make computations tractable, the multiscale models generally make use of a coarse-fine grain decomposition for the physical domain under analysis. An atomistic simulation method is used in a small subregion, the fine grain, where it is crucial to capture the individual atomistic behavior accurately. A continuum simulation is used in a larger peripheral region, the coarse grain, where the deformation is considered to be homogeneous and smooth; the macroscopic material behavior and properties are mainly determined by the collective atomic motion. Since the continuum region is usually chosen to be much larger than the atomistic region, the overall domain of interest can be considerably large. A purely atomistic solution is normally not affordable on this domain, though the multiscale solution would presumably provide the detailed atomistic information only when and where it is necessary.

The key issue is then the coupling between the coarse and fine scales. An approximation is necessary along the fine-coarse grain interface, due to the fundamental incompatibility of the atomistic and continuum descriptions (e.g., Deymier and Vasseur, 2002). This incompatibility is imposed by mismatch of the dispersion characteristics of the continuous and discrete media in dynamic simulations, and by the non-local character of the atomic interaction in dynamic and quasistatic simulations. Typically, the concurrent coupling involves the idea of a "handshake" or "pad" region, e.g., Curtin and Miller (2003), Liu et al. (2004), Shilkrot et al. (2004), Broughton et al. (1999), Abraham et al. (1998), Rudd and Broughton (1998, 2000), Tadmor et al. (1996), Shenoy et al. (1998) and Ortiz et al., 2001, where pseudoatoms are available on the continuum part of the interface and share the physical space with finite elements, as shown in Fig. 1. At the front end of the continuum interface, the finite elements have to be scaled down to the atomic bond lengths. The purpose of the handshake region is to assure smoother coupling between the atomistic and continuum regimes. The group of pseudoatoms serves to eliminate the non-physical surface in the atomistic lattice structure, so that
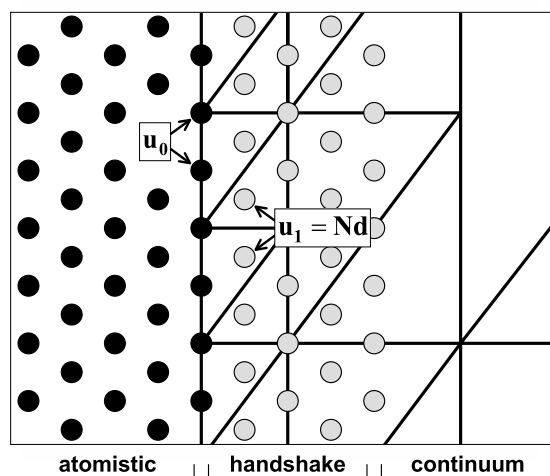

Fig. 1. Structure of the transition region in coupled atomistic/continuum simulations. Positions of pseudoatoms in the handshake area are interpolated with finite element shape functions.

the real atoms along the interface have a full set of interactive neighbors in the continuum domain. In dynamic simulations, the handshake also serves as a damper/absorbent to reduce the spurious reflection of high frequency phonons that cannot pass into the coarse scale domain. However, this reflection can be eliminated only partially by a reasonably sized handshake domain. Besides, introduction of a non-physical handshake region leads to the three other concerns in both dynamic and quasistatic modelling. The *first* is double counting of the strain energy in the handshake region by the atomistic and continuum models. The *second* is ill-conditioning of the finite element stiffness matrices, due to the need in atomic length scale refinement of the finite element mesh for the handshake region. Indeed, an extremely fine mesh is required in order to provide accurate positions of the pseudoatoms, since they are found by interpolating the finite element nodal positions (Curtin and Miller, 2003). Note that the FE interpolation procedure can be written symbolically,

$$\mathbf{u}_1 = \mathbf{Nd} \tag{1}$$

where $\mathbf{u}_1$ are displacements of the pseudoatoms interacting with the interface atoms, $\mathbf{d}$ are finite element nodal displacements, and the columns of the rectangular matrix $\mathbf{N}$ give a set of interpolation basis vectors, computed by utilizing the FE shape functions. And the *third* concern is related to the need in a non-local continuum model for the small length scales that are typical for the handshake region.

An alternative methodology has been proposed recently for dynamic simulations (Karpov et al., 2005, 2004; Park et al., 2005a), where positions of actual next-to-interface atoms from the coarse grain are computed by means of a functional operator over displacements of the interfacial atoms. This operator essentially relates the displacements of coarse grain atoms interacting with the interface, $\mathbf{u}_1$, and the interface atomic displacements, $\mathbf{u}_0$, as $\mathbf{u}_1 = \Theta\{\mathbf{u}_0\}$ at all times. Here and further, all atomic displacements are implied about equilibrium positions in the ideal crystal lattice. The derivation of the interface operator Θ is a straightforward semi-analytical procedure based on the Fourier analysis of periodic lattice structures (Karpov et al., 2002; Karpov et al., 2003; Ryvkin et al., 1999), which provides the required solution at the intrinsic atomistic level. For linear coarse grains with regular crystalline interfaces, this operator was shown to act as a convolution integral with a compact and spatially invariant kernel function of time. However, this model is only applicable to the case of *infinite* coarse grains. Here, infiniteness of the coarse grain is understood in the sense that the progressive waves caused by the peripheral boundary conditions do not reach the fine-coarse grain interface during the prescribed simulation time. In other words, this approach is applicable to problems with only inner (fine grain) excitations of the time-dependent deformation; examples are heat transfer in contact problems, dynamic nanoindentation and deposition problems.

One interesting approach to atomistic-continuum coupling is the bridging scale method (Wagner and Liu, 2003; Park et al., 2005b,c). This method employs the dynamic multiscale boundary conditions to give a force $\mathbf{f}_{1\to0}$ exerted on the interface atoms from the side of all the coarse grain atoms eliminated from the explicit consideration. In principle, this force is computed based on the displacements $\mathbf{u}_0$ and $\mathbf{u}_1$, where $\mathbf{u}_1 = \Theta\{\mathbf{u}_0\}$. The force $\mathbf{f}_{1\to0}$ is also called the lattice impedance force, because it represents the dynamic response characteristics of a crystal lattice along a fine/coarse grain interface. The original form of this method was presented for the case of short range potentials, where it did not require a handshake domain. However, the long-range atomic forces may still impose a small overlapping domain, and therefore double counting of the strain energy, within the effective range of these forces.

The handshake and continuum domains serve to absorb the fine grain excitations and to transfer effects of the peripheral (coarse grain) boundary into the central atomistic region of interest. In principle, this requires evaluation of the displacement vector $\mathbf{u}_1$, as depending on the interface displacements $\mathbf{u}_0$ and the peripheral boundary displacements $\mathbf{u}_a$ (a is a coarse grain size parameter) at each step of the solution procedure. This dependence can be written in the symbolic form,

$$\mathbf{u}_1 = \Theta\{\mathbf{u}_0\} + \Xi\{\mathbf{u}_a\} \tag{2}$$

that gives the *multiscale boundary conditions* for the atomistic model on the fine grain (see Fig. 2). Here, Θ and Ξ are unknown mathematical operators to be determined. In principle, if both of these operators were known from alternative arguments, for example, employing the methods of lattice mechanics, the explicit continuum model, as well as the handshake domain would become redundant.
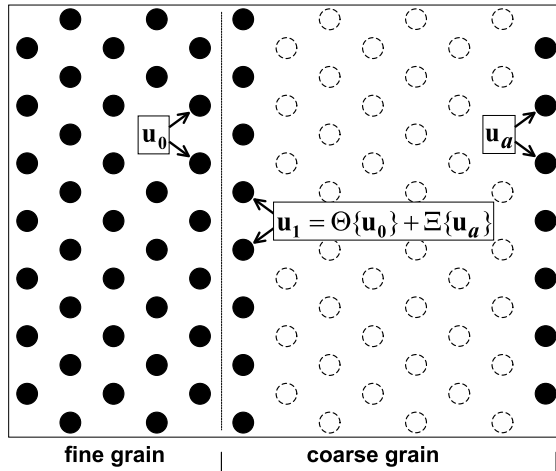
Fig. 2. Multiscale boundary conditions: atomic positions on a coarse grain are evaluated through the displacements of atoms at the interface and the coarse grain's outer boundary. Explicit continuum modeling is not involved.

In this paper we demonstrate a semi-analytical method to derive the complete multiscale boundary conditions for crystalline solids, expressed by Eq. (2). This first effort is presented within the quasistatic settings. The method is based on the intrinsic crystal structure model, without involving a continuum homogenization procedure. Fig. 2 and Eq. (2) represent the basic idea and the major distinctive feature of the present approach, as compared with the available multiscale methods that utilize a finite element interpolation of the type (1). Section 2 of this paper provides a systematic consideration of multiscale boundary conditions in one-dimensional (1D), or "beam-like", lattices. Section 3 extends this formulation to an arbitrary three-dimensional (3D) crystal structure. The method is verified on a series of illustrative 3D nanoindentation simulations with crystalline gold substrates in Section 4. Section 5 concludes the paper.

2. One-dimensional periodic lattices

2.1. Monoatomic chain

We start the discussion with the simplest periodic lattice, the 1D monoatomic atomic chain depicted in Fig. 3. This example is used in order to detail the idea of multiscale boundary conditions. Assume that each atom has a single, longitudinal degree of freedom, and that it only interacts with its nearest neighbors. This interaction is described by a linear spring stiffness k. The fine grain boundary atom 0 is subjected to a known force **f** due to some atomistic process on the left and the response of a coarse grain on the right. Atom a represents the peripheral boundary of the coarse grain, and its displacement is provided. Then, the solution for the interface atoms 0 and 1 can be computed without solving the entire coarse grain, provided that a relationship among the displacements of atoms 0, 1 and a, as manifested by Eq. (2), is established. Indeed, Eq. (2)
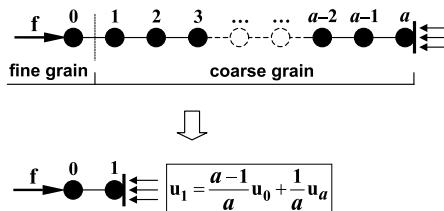

Fig. 3. Multiscale boundary conditions: atomic positions on a coarse grain are evaluated through the displacements of atoms at the interface and the coarse grain's outer boundary. Explicit continuum modeling is not involved.

solved simultaneously with the force/displacement relationship, $k(\mathbf{u}_1 - \mathbf{u}_0) = -\mathbf{f}$, provides unique displacements $\mathbf{u}_0$ and $\mathbf{u}_1$. Eq. (2) contains two mathematical operators Θ and Ξ, whose form depends on the lattice properties and the coarse scale size parameter a. Technically, the objective of this paper is to provide a general approach to deriving these operators for arbitrary periodic lattice structures.

The periodicity of the monoatomic chain implies a uniform character of the equilibrium deformation under static end loadings, so that

$$\mathbf{u}_1 = \frac{a-1}{a}\mathbf{u}_0 + \frac{1}{a}\mathbf{u}_a \tag{3}$$

for arbitrary displacements $\mathbf{u}_0$ and $\mathbf{u}_a$. This formula can be obtained based on elementary arguments: the sought displacement $\mathbf{u}_1$ is given by a first order interpolation polynomial, satisfying the sample values $\mathbf{u}_0$ and $\mathbf{u}_a$ at $x = 0$ and $x = a$, and then evaluated at $x = 1$.

In principle, Eq. (3) represents the multiscale boundary condition for the monoatomic 1D chain. It can be regarded as an additional equation for the boundary degree of freedom, $\mathbf{u}_1$, and solved *simultaneously* with general molecular mechanics equations for the fine grain degrees of freedom, i.e., displacements $\mathbf{u}_n$ at $n < 1$. The resultant solution will automatically incorporate the effect of the peripheral degrees of freedom, $\mathbf{u}_n$ at $n = 1, 2, \ldots, a$.

We emphasize that atom 1 will then serve as the actual boundary of the computational domain, though its displacement must be updated at *each step* of the molecular mechanics energy minimization procedure. The displacement of the boundary atom 1 will be determined by both the peripheral and local effects; we will refer to such an atom or group of atoms (in two- and three-dimensional applications) as the *multiscale boundary*. For more complicated periodic structures, the multiscale boundary conditions can be evaluated on the basis of discrete Fourier transform, as discussed in below Sections 2.2 and 3.

2.2. Arbitrary beam-like lattices

In this section, we consider a general beam-like lattice, i.e., an arbitrary structure formed by translating a small group of atoms (the unit cell) along one spatial axis equidistantly. Examples are shown in Fig. 4. Each repetitive cell is associated with a unique integer value of the spatial index n, as well as with the Cartesian vectors of atomic displacements and external forces, $\mathbf{u}_n$ and $\mathbf{f}_n^{\text{ext}}$. The length of these vectors is defined by the number of atomistic degrees of freedom in one repetitive cell. In principle, the problem of solving for the vector $\mathbf{u}_1$ in terms of $\mathbf{u}_0$ and $\mathbf{u}_a$ is equivalent to solving the boundary value problem for the lattice structure $n = 0, 1, \ldots, a$, and then writing the solution for the cell $n = 1$. In contrast to the above example of a monoatomic 1D chain, no intuitive arguments can be found for a structure with multiple degrees of freedom per unit cell. A consistent semi-analytical approach to solving this problem is discussed below.

The static equilibrium equation for regular beam-like lattices with a first order atomic force approximation can be written for a repetitive atomic cell n in terms of the discrete convolution summation,

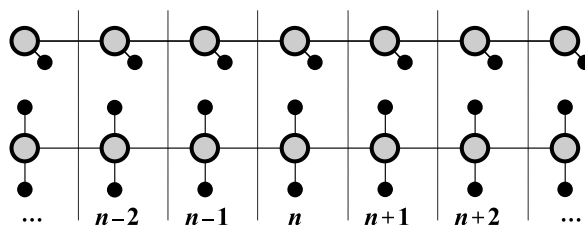$$\sum_{n'=n-1}^{n+1} \mathbf{K}_{n-n'}\mathbf{u}_{n'} = -\mathbf{f}_n, \quad n = 1, \ldots, a - 1 \tag{4}$$

Fig. 4. Numbering of repetitive cells in periodic beam-like lattices.

where $\mathbf{u}$ and $\mathbf{f}$ are s-component vectors of displacements and external forces in the corresponding unit cells, s is the number of degrees of freedom in one cell; $\mathbf{u}_0$ and $\mathbf{u}_a$ are viewed as the boundary conditions. Since the coarse grain is free of in-domain external loads, the force vector for this equation is given by

$$\mathbf{f}_n = \delta_{n,0}\mathbf{f}_0 + \delta_{n,a}\mathbf{f}_a, \quad n = 0, 1, \ldots, a \tag{5}$$

where δ is the Kronecker delta, and $\mathbf{f}_0$, $\mathbf{f}_a$ are unknown boundary forces. Eq. (4) assumes that each cell n interacts only with two adjacent cells $n - 1$ and $n + 1$. The K-matrices in (4) represent elastic properties of the lattice structure. They can be expressed through the potential energy of the lattice, U, utilized in terms of the displacements about equilibrium positions

$$\mathbf{K}_{n-n'} = -\frac{\partial^2 U(\mathbf{u})}{\partial \mathbf{u}_n \, \partial \mathbf{u}_{n'}}\bigg|_{\mathbf{u}=0} \tag{6}$$

Obviously, the matrices $\mathbf{K}_{n-n'}$ are invariant with respect to n in a regular lattice; therefore this procedure has to be accomplished only once—for an arbitrary cell n to yield three non-trivial matrices $\mathbf{K}_{-1}$, $\mathbf{K}_0$ and $\mathbf{K}_1$.

The governing equation (4) gives a coupled system of linear finite difference equations, which can be solved *selectively* for $\mathbf{u}_1$ by adapting the discrete Fourier transform method (e.g., Karpov et al., 2002, 2003). The discrete Fourier transform of a sequence of numbers, vectors, or matrices g_n is defined as the sum over all non-trivial elements of this sequence,

$$\hat{g}(p) = \mathscr{F}_{n \to p}\{g_n\} = \sum_{n=n_{\min}}^{n_{\max}} g_n \mathrm{e}^{-\mathrm{i}pn}, \quad p \in [-\pi, \pi] \tag{7}$$

Here, the hatted notation $\hat{g}$ stands for the Fourier images, $n_{\min}$ and $n_{\max}$ are the minimal and maximal values of the integer index n for a given sequence, and the calligraphic symbols $\mathscr{F}$ denotes the Fourier transform operator. The inversion formula is given by

$$g_n = \mathscr{F}_{p \to n}^{-1}\{\hat{g}(p)\} = \frac{1}{2N} \sum_{v_p=1/2-N}^{N-1/2} \hat{g}\left(\frac{\pi v_p}{N}\right)\mathrm{e}^{\mathrm{i}\pi v_p n/N} \tag{8}$$

Here, the semi-integer summation index v_p is utilized, and the value $2N$ gives the domain's size, or length of the sequence $g_n : n_{\max} - n_{\min} + 1$. For the present problem, we have $2N = a + 1$ that gives a lateral size of the coarse grain in unit cells. Derivation of the formula (8) and the relevant discussion are provided in Appendix A. For the purpose of further discussion, we recall two properties of the DFT: the convolution and shift theorems (proves are provided in Appendix A),

$$\mathscr{F}\left\{\sum_{n'} f_{n-n'} g_{n'}\right\} = \hat{f}(p)\hat{g}(p) \tag{9}$$

$$\mathscr{F}\{g_{n+h}\} = \hat{g}(p)\mathrm{e}^{\mathrm{i}hp}, \tag{10}$$

where h is integer. Applying the discrete Fourier transform (7) over Eq. (4), and taking into account the convolution theorem (9), we obtain

$$\hat{\mathbf{K}}(p)\hat{\mathbf{u}}(p) = -\hat{\mathbf{f}}(p) \tag{11}$$

Hence, the Fourier domain solution reads

$$\hat{\mathbf{u}}(p) = -\hat{\mathbf{K}}^{-1}(p)\hat{\mathbf{f}}(p) \tag{12}$$

Next we apply the inverse DFT with the convolution theorem to (12), and utilize the force vector (5). This gives the real-space displacement vector $\mathbf{u}$ in terms of the n-parametric $s \times s$ matrix $\mathbf{G}$ called the lattice Green's function (Karpov et al., 2002, 2003)

$$\mathbf{u}_n = \sum_{n'=0}^{a} \mathbf{G}_{n-n'}\mathbf{f}_{n'} = \mathbf{G}_n\mathbf{f}_0 + \mathbf{G}_{n-a}\mathbf{f}_a, \quad n = 0, 1, \ldots, a \tag{13}$$

$$\mathbf{G}_n = \frac{1}{2N} \sum_{v_p=1/2-N}^{N-1/2} \hat{\mathbf{G}}\left(\frac{\pi v_p}{N}\right) e^{i\pi v_p n/N}, \quad N = \frac{a+1}{2} \tag{14}$$

Here,

$$\hat{\mathbf{G}}(p) = -\hat{\mathbf{K}}^{-1}(p) \equiv -(\mathscr{F}\{\mathbf{K}_n\})^{-1} = -\left(\mathbf{K}_{-1}e^{ip} + \mathbf{K}_0 + \mathbf{K}_1 e^{-ip}\right)^{-1} \tag{15}$$

Next we write the displacement vector, expressed by Eq. (13), at $n = 0$, $n = 1$ and $n = a$,

$$\mathbf{u}_0 = \mathbf{G}_0\mathbf{f}_0 + \mathbf{G}_{-a}\mathbf{f}_a$$
$$\mathbf{u}_1 = \mathbf{G}_1\mathbf{f}_0 + \mathbf{G}_{1-a}\mathbf{f}_a \tag{16}$$
$$\mathbf{u}_a = \mathbf{G}_a\mathbf{f}_0 + \mathbf{G}_0\mathbf{f}_a$$

and express the unknown force vectors $\mathbf{f}_0$ and $\mathbf{f}_a$ in terms of $\mathbf{u}_0$ and $\mathbf{u}_a$ using the first and the third equations of (16)

$$\begin{pmatrix} \mathbf{f}_0 \\ \mathbf{f}_a \end{pmatrix} = \begin{pmatrix} \mathbf{G}_0 & \mathbf{G}_{-a} \\ \mathbf{G}_a & \mathbf{G}_0 \end{pmatrix}^{-1} \begin{pmatrix} \mathbf{u}_0 \\ \mathbf{u}_a \end{pmatrix} \tag{17}$$

Finally, we employ the external force vectors (17) in the second equation of (16) to obtain the general 1D multiscale boundary condition in the matrix form

$$\mathbf{u}_1 = \mathbf{\Theta}\mathbf{u}_0 + \mathbf{\Xi}\mathbf{u}_a \tag{18}$$

$$(\mathbf{\Theta} \quad \mathbf{\Xi}) = (\mathbf{G}_1 \quad \mathbf{G}_{1-a}) \begin{pmatrix} \mathbf{G}_0 & \mathbf{G}_{-a} \\ \mathbf{G}_a & \mathbf{G}_0 \end{pmatrix}^{-1} \tag{19}$$

Thus, the sought operators of multiscale boundary conditions for beam-like lattices are $s \times s$ square matrices defined solely by the interatomic potential and the coarse scale parameter a. We note that the matrix $\mathbf{G}_n$, Eq. (14), is evaluated only at $n = -a$, $1 - a$, 0, and 1. The cost of such an inverse DFT procedure is only $\sim N^1$, so that relatively large linear dimensions of the coarse scale domain will be accessible with the usage of modern computers (up to $a \approx 10^4, \ldots, 10^7$, depending on complexity of the unit cell).

This formulation can be verified on the 1D lattice example discussed in Section 2.1, where each repetitive cell is represented by a single atom with one longitudinal degree of freedom. This example is unique in allowing elementary arguments to write the multiscale boundary conditions, presented by Eq. (3). The K-matrices for this problem reduce to the scalar quantities

$$\mathbf{K}_{\pm 1} = k, \quad \mathbf{K}_0 = -2k \tag{20}$$

where k is the linear interaction coefficient. The transform domain Green's function (15), in application to this structure, gives $\hat{\mathbf{G}}(p) = (2 - 2\cos p)^{-1}$ at $k = 1$. The real space function (14) can be computed numerically by utilizing various $n \in [-2N, 2N]$; these calculations yield

$$\mathbf{G}_n = \frac{1}{4N} \sum_{v_p=1/2-N}^{N-1/2} \frac{e^{i\pi v_p n/N}}{1 - \cos(\pi v_p/N)} = \frac{N - |n|}{2}, \quad |n| < 2N \tag{21}$$

Substituting the required values of the Green's function (21) into Eq. (19) gives

$$(\mathbf{\Theta} \quad \mathbf{\Xi}) = (N - 1 \quad N + 1 - a) \begin{pmatrix} N & N - a \\ N - a & N \end{pmatrix}^{-1} \tag{22}$$

$$(\mathbf{\Theta} \quad \mathbf{\Xi}) = \left(\frac{a-1}{a} \quad \frac{1}{a}\right) \tag{23}$$

The DFT inversion parameter N cancels in (22), and the final result (23) is equivalent to the earlier formula (3).

3. Three-dimensional crystal lattices

In this section we derive the multiscale boundary conditions for three-dimensional systems by generalizing the results of Section 2.2. Typically, a fine/coarse grain interface in a 3D crystal structure is characterized by a regularity of spatial arrangement of repetitive cells identified with triplets of indices (n, m, l); an example is shown in Fig. 5. An assumption required for obtaining a straightforward extension to the 3D formalism is that the fine/coarse grain interface can be comprised by a group of *plane-* or *slab-like* interfaces. Each of these interfaces is to be treated according to the below formulation. This assumption, in principle, imposes limitations on allowed shapes of the fine grain, which is expected in the form of a convex polyhedron, though not necessarily regular. Since the fine grain is only a *computational* domain, which is not required to represent an element of intrinsic physical structure of the solid, this assumption is considered as acceptable. In particular, this assumption is satisfactory for applications with the emphasis on behavior and properties of the fine scale domain, where bulk domain geometry does not play a major role; we note that the peripheral boundaries within the present assumption will conform to a similar planar setup as the fine scale domain. Examples of such applications are the nanoindentation simulations considered in this paper, and the deformation of large periodic nanostructures, such as carbon nanotubes and graphene monolayers, with a localized region of interest. In case that the coarse grain geometry is of major interest, as in geometry optimization and design of engineering nanostructures and parts of nanoscale machines, the *hybrid* molecular mechanics/FEM methodologies can be more relevant than the present method. Examples of such hybrid techniques are the works by Abraham et al. (1998), Rudd and Broughton (1998, 2000), Ortiz et al. (2001) and Park et al. (2005b,c). Meanwhile, the major advantages of the present approach are the simplicity of the formulation and the straightforward implementation for a readily available molecular mechanics code; in greater detail, the algorithmic issues are discussed in Section 4.

The three-dimensional generalization of governing equation (4) gives

$$\sum_{n'=n-\nu}^{n+\nu} \sum_{m'=m-\mu}^{m+\mu} \sum_{l'=l-1}^{l+1} \mathbf{K}_{n-n',m-m',l-l'} \mathbf{u}_{n',m',l'} = -\mathbf{f}_{n,m,l} \tag{24}$$

where "l" is the direction from the interface towards the peripheral coarse grain boundary, and the three-dimensional K-matrices are defined according to

$$\mathbf{K}_{n-n',m-m',l-l'} = -\frac{\partial^2 U(\mathbf{u})}{\partial \mathbf{u}_{n,m,l} \partial \mathbf{u}_{n',m',l'}}\bigg|_{\mathbf{u}=0} \tag{25}$$

to relate the displacements in the cells (n', m', l') to the forces in the current cell (n, m, l). By symmetry of the partial derivatives, $\mathbf{K}_{-n,-m,-l} = \mathbf{K}_{n,m,l}^{\mathrm{T}}$.
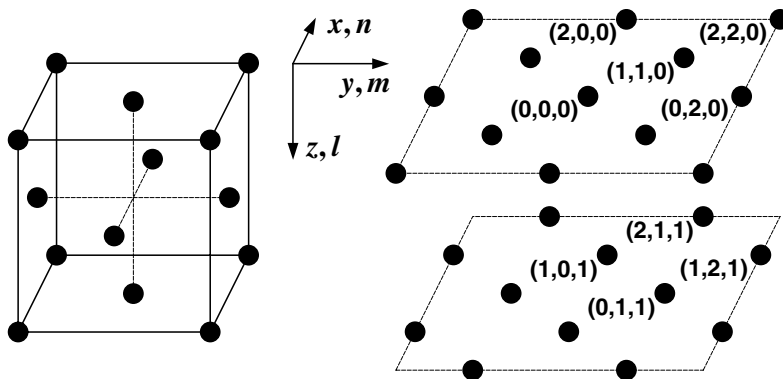

Fig. 5. Face centered cubic crystal: Bravais lattice structure (left); numbering of equilibrium atomic positions (n, m, l) in two adjacent $(0\,0\,1)$ planes, corresponding to $l = 0$ and $l = 1$ (right). Interplanar distance is exaggerated.

Note the distinct character of the third summation in Eq. (24) as compared to the first and second. For the analysis to follow, we require that the atoms in a given slab of constant l are coupled only to each other and to atoms in the slabs $l-1$ and $l+1$. For longer-range forces, the size of the unit cell must be increased so that this requirement is satisfied. At the same time, the coupling in the directions of indices n and m is not limited to immediate neighbors, and the parameters ν and μ of (24) indicate the corresponding maximum order numbers of the interactive cells.

Thus, the task of deriving the 3D multiscale boundary conditions reduces to expressing the atomic displacements $\mathbf{u}_{n,m,1}$ in terms of $\mathbf{u}_{n,m,0}$ and $\mathbf{u}_{n,m,a}$,

$$\mathbf{u}_{n,m,1} = \Theta\{\mathbf{u}_{n,m,0}\} + \Xi\{\mathbf{u}_{n,m,a}\} \tag{26}$$

where slab $l=0$ represents the fine/coarse grain interface, and $l=a$ assigns the coarse grain boundary.

Similarly to the 1D case, discussed in Section 2.2, the coarse grain deformation is viewed as due to the external forces applied to the atoms $(n,m,0)$ and (n,m,a)

$$\mathbf{f}_{n,m,l} = \delta_{l,0}\mathbf{f}_{n,m,0} + \delta_{l,a}\mathbf{f}_{n,m,a} \tag{27}$$

Next we apply the DFT to Eq. (24) for all three spatial indices, utilizing the external force vector (27) and the convolution theorem (9) to get the Fourier domain solution

$$\hat{\mathbf{u}}(p,q,r) = \hat{\mathbf{G}}(p,q,r)\Big(\hat{\mathbf{f}}_0(p,q) + \mathrm{e}^{-ira}\hat{\mathbf{f}}_a(p,q)\Big) \tag{28}$$

$$\hat{\mathbf{G}}(p,q,r) = -\hat{\mathbf{K}}^{-1}(p,q,r) \tag{29}$$

We note that within the 3D settings, the DFT can only be utilized for up to three linearly independent spatial directions; attempts to implement it along additional (linearly dependent) directions may lead to trivial results. Further use of the shift theorem (10) with the inverse $(r \to l)$ DFT applied to Eq. (28) yields

$$\tilde{\mathbf{u}}_l(p,q) = \tilde{\mathbf{G}}_l(p,q)\mathbf{f}_0(p,q) + \tilde{\mathbf{G}}_{l-a}(p,q)\mathbf{f}_a(p,q) \tag{30}$$

$$\tilde{\mathbf{G}}_l(p,q) = \mathscr{F}_{r \to l}^{-1}\{\hat{\mathbf{G}}(p,q,r)\} \tag{31}$$

where the tilde notations represent the mixed, Fourier/real space, domain quantities; the $(r \to l)$ inverse Fourier transformation is accomplished in accordance with (8), where p, n and N are replaced with r, l and $L = (a+1)/2$, respectively.

Then we write three equations according to (30) by substituting $l=0$, $l=1$ and $l=a$, and rearrange them to express the vector $\tilde{\mathbf{u}}_1$ through $\tilde{\mathbf{u}}_0$ and $\tilde{\mathbf{u}}_a$

$$\tilde{\mathbf{u}}_1(p,q) = \hat{\boldsymbol{\Theta}}(p,q)\tilde{\mathbf{u}}_0(p,q) + \hat{\boldsymbol{\Xi}}(p,q)\tilde{\mathbf{u}}_a(p,q) \tag{32}$$

where

$$\big(\hat{\boldsymbol{\Theta}}(p,q) \quad \hat{\boldsymbol{\Xi}}(p,q)\big) = \big(\tilde{\mathbf{G}}_1(p,q) \quad \tilde{\mathbf{G}}_{1-a}(p,q)\big)\begin{pmatrix} \tilde{\mathbf{G}}_0(p,q) & \tilde{\mathbf{G}}_{-a}(p,q) \\ \tilde{\mathbf{G}}_a(p,q) & \tilde{\mathbf{G}}_0(p,q) \end{pmatrix}^{-1} \tag{33}$$

Here, we note the similarity of the 3D Fourier domain equations (32) and (33) with the 1D real space equations (18) and (19).

By applying the inverse DFT for p and q to Eq. (32), and taking into account the convolution theorem (9), we obtain the final form of the 3D multiscale boundary conditions

$$\mathbf{u}_{n,m,1} = \sum_{n',m'} \boldsymbol{\Theta}_{n-n',m-m'}\mathbf{u}_{n',m',0} + \sum_{n',m'} \boldsymbol{\Xi}_{n-n',m-m'}\mathbf{u}_{n',m',a} \tag{34}$$

$$\boldsymbol{\Theta}_{n,m} = \mathscr{F}_{p \to n}^{-1}\mathscr{F}_{q \to m}^{-1}\{\hat{\boldsymbol{\Theta}}(p,q)\}, \quad \boldsymbol{\Xi}_{n,m} = \mathscr{F}_{p \to n}^{-1}\mathscr{F}_{q \to m}^{-1}\{\hat{\boldsymbol{\Xi}}(p,q)\} \tag{35}$$

The range of the summation indices for computing the inverse DFTs in (35), $p \in [1/2 - N, N - 1/2]$ and $q \in [1/2 - M, M - 1/2]$, must be such that values $2N$ and $2M$ match or exceed lateral dimensions of the coarse grain along the n and m directions. Then periodic boundary conditions for n and m can be safely assumed.

Thus, the three-dimensional operators of multiscale boundary conditions act as discrete convolution sums over the interface and coarse grain boundary displacements. These operators are represented by the compact matrix kernels $\boldsymbol{\Theta}$ and $\boldsymbol{\Xi}$ depending on the lattice geometry and structure of the interatomic potential.

In some applications, including the nanoindentation simulations to be discussed later in this paper, the coarse scale boundary can be assumed rigidly fixed, so that $\mathbf{u}_{n,m,a} = \mathbf{0}$ for all n and m. This assumption simplifies Eq. (34) to the form

$$\mathbf{u}_{n,m,1} = \sum_{n',m'} \boldsymbol{\Theta}_{n-n',m-m'} \mathbf{u}_{n',m',0} \qquad (36)$$

In conclusion of this theoretical section, we emphasize that the kernel matrices $\boldsymbol{\Theta}$ and $\boldsymbol{\Xi}$ are *dimensionless* quantities, because they relate ''displacements with displacements'', according to (34) and (36). This indicates that, for a given interatomic potential, their values should depend on the geometry of the crystal lattice and the choice of the elementary cell, rather than on scaling parameters of this potential. This feature is attractive, because it implies the existence of unique kernel matrices for various materials with identical or similar crystalline structures.

4. Application: nanoindentation of crystalline gold

In this section we verify the three-dimensional formulation on two benchmark nanoindentation problems with a crystalline gold substrate. For illustrative purposes, we will consider two parallelopipedic configurations of the fine grain: (1) with periodic boundary conditions on the side faces, and the multiscale boundary conditions on the bottom face (Example 1), and (2) with multiscale boundary conditions at five faces (Example 2). The top face of the fine grain domain is originally traction free, and it is next subjected to a non-deformable indenter. The first of these geometries represent the simplest case that is equivalent to dealing with a single, formally infinite, plane interface, and the second geometry represents an example of compound interfaces mentioned in the beginning of Section 3.

A substantial part of the substrate is considered as a bulk coarse scale domain, whose atomistic degrees of freedom will be eliminated from the multiscale model. The resultant multiscale solution will be compared with the benchmark data, obtained by molecular mechanics simulations on the original full domain, i.e., by preserving the complete atomistic resolution and all the relevant degrees of freedom at both fine and coarse grains. The coarse scale boundary displacements in both problems are set to be zero; therefore Eq. (36) will be utilized.

We introduce the three-dimensional numbering of the atomic locations in the fcc lattice, so that the atoms occupy the even staggered locations (n,m,l) as illustrated in Fig. 5. Planes with a constant value n, m or l are coplanar with the crystallographic planes $(1\,0\,0)$, $(0\,1\,0)$ or $(0\,0\,1)$, respectively. We assume the pair-wise Morse potential for the atomic interactions in gold (e.g., Harrison, 1988)

$$\begin{aligned} &V(r) = D_e\left[e^{2\beta(\rho-r)} - 2e^{\beta(\rho-r)}\right] \\ &D_e = 0.560\,\text{eV}, \quad \beta = 1.637\,\text{Å}^{-1}, \quad \rho = 2.922\,\text{Å} \end{aligned} \qquad (37)$$

and will account only for the nearest neighbor interaction in the fcc lattice. In this case, the lattice unit cells are represented by single atoms numbered as shown in Fig. 5. For the Cartesian frame depicted in this figure, we obtain the following set of symmetric K-matrices on the basis of expression (25):

$$\mathbf{K}_{1,1,0} = k\begin{pmatrix} 1 & 1 & 0 \\ 1 & 1 & 0 \\ 0 & 0 & 0 \end{pmatrix}, \quad \mathbf{K}_{1,-1,0} = k\begin{pmatrix} 1 & -1 & 0 \\ -1 & 1 & 0 \\ 0 & 0 & 0 \end{pmatrix}$$

$$\mathbf{K}_{1,0,1} = k\begin{pmatrix} 1 & 0 & 1 \\ 0 & 0 & 0 \\ 1 & 0 & 1 \end{pmatrix}, \quad \mathbf{K}_{1,0,-1} = k\begin{pmatrix} 1 & 0 & -1 \\ 0 & 0 & 0 \\ -1 & 0 & 1 \end{pmatrix}$$

$$\mathbf{K}_{0,1,1} = k \begin{pmatrix} 0 & 0 & 0 \\ 0 & 1 & 1 \\ 0 & 1 & 1 \end{pmatrix}, \quad \mathbf{K}_{0,1,-1} = k \begin{pmatrix} 0 & 0 & 0 \\ 0 & 1 & -1 \\ 0 & -1 & 1 \end{pmatrix}$$

$$\mathbf{K}_{0,0,0} = -8k \begin{pmatrix} 1 & 0 & 0 \\ 0 & 1 & 0 \\ 0 & 0 & 1 \end{pmatrix}, \quad k = D_e \beta^2 \tag{38}$$

In greater detail, derivation of these matrices is discussed in Appendix A. Six additional matrices are obtained from (38) by employing $\mathbf{K}_{-n,-m,-l} = \mathbf{K}_{n,m,l}$, while any other subscript triplet (n, m, l) yields a zero matrix. The Fourier transform (7) of these matrices can be derived in a closed form

$$\hat{\mathbf{K}}(p,q,r) = 4k \begin{pmatrix} (\cos q + \cos r)\cos p & -\sin p \sin q & -\sin p \sin r \\ -\sin p \sin q & (\cos p + \cos r)\cos q & -\sin q \sin r \\ -\sin p \sin r & -\sin q \sin r & (\cos p + \cos q)\cos r \end{pmatrix} - 8k\mathbf{I} \tag{39}$$

where $\mathbf{I}$ is the identity matrix.

Further steps in computing the kernel matrix $\mathbf{\Theta}$ are accomplished numerically, according to the procedures (29), (31), (33), (35), and the DFT inversion formula (8).

Elements of the matrix $\mathbf{\Theta}$ decay quickly with the increase of absolute values of the spatial order parameters n and m. We illustrate this property by plotting element $(1, 1)$ of this matrix in Fig. 6, as a representative function of n at $a = 15$, the coarse scale parameter, and various m. The overall trends shown are typical for all other elements of $\mathbf{\Theta}$. In accordance with the staggered atomic arrangements in the fcc crystal, matrices $\mathbf{\Theta}$ for even $n + m$ appear trivial, and they are ignored in Fig. 6 plot. The value of the element $(1, 1)$ is seen to decay by a factor of 100 with the growth of $|n|$ or $|m|$ from 0 to 4. This decay is a valuable property of the kernel matrix. Taking it into account, we can truncate the summation in Eq. (36) at some critical differences $n - n'$ and $m - m'$ without a considerable loss of the accuracy. By denoting these critical values as n_c and m_c, we can update Eq. (36) to give the final form,

$$\mathbf{u}_{n,m,1} = \sum_{n'=n-n_c}^{n+n_c} \sum_{m'=m-m_c}^{m+m_c} \mathbf{\Theta}_{n-n',m-m'} \mathbf{u}_{n',m',0} \equiv \mathbf{\Theta} * \mathbf{u}_{n,m,0} \tag{40}$$

that has been utilized in our simulations. In most applications with the present fcc model, it is proper to truncate this convolution sum at n_c, $m_c = 4$–6. This truncation can notably decrease computational cost of the multiscale boundary conditions.
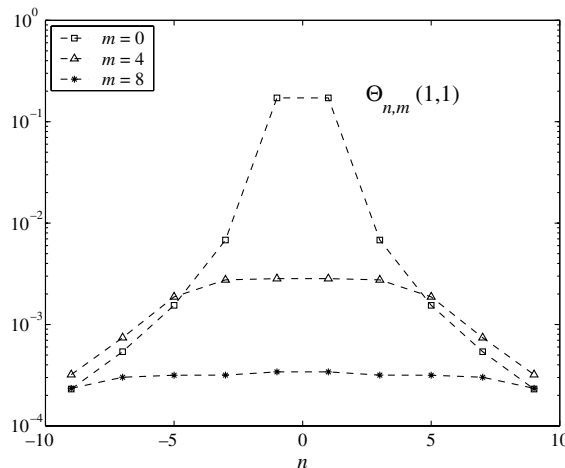

Fig. 6. Typical dependence of the components in the kernel matrix on the values of spatial order parameters.

Another important feature of this kernel matrix is that it is *invariant* with respect to the value of the interaction coefficient k in matrices (38), and therefore with respect to parameters of pair-wise potentials. Thus, the present kernel matrix Θ for a given value a is a general characteristic of all monoatomic fcc crystals with the nearest neighbor interaction.

4.1. Algorithmic issues

The conditions (40) provide additional equations for the degrees of freedom at the boundary of the reduced domain that must be solved *simultaneously* with the standard molecular mechanics equations for the inner part of the reduced domain. Below, we discuss two possible approaches to such a simultaneous solution. The first approach consists in replacing the vectors $\mathbf{u}_{n,m,1}$ in the argument of the system's potential energy function U with the convolution sums (40),

$$U(\ldots, \mathbf{u}_{n,m,-1}, \mathbf{u}_{n,m,0}, \mathbf{u}_{n,m,1}) \rightarrow U_{\mathrm{MS}}(\ldots, \mathbf{u}_{n,m,-1}, \mathbf{u}_{n,m,0}, \Theta * \mathbf{u}_{n,m,0}) \tag{41}$$

for each specific pair of indices n and m. The new function U_{MS} is then sent to a minimization subroutine available in any standard molecular mechanics code. With this approach, the multiscale boundary displacements $\mathbf{u}_{n,m,1}$ will be updated automatically at each iteration step of the energy minimization procedure.

The second approach that we suggest does not involve an update of the potential energy function; instead, it treats specific displacements (40) evaluated at a current iteration step of the minimization process as boundary conditions for the next step

$$\text{Step } j: \ U(\ldots, \mathbf{u}_{n,m,-1}, \mathbf{u}_{n,m,0}, \mathbf{u}_{n,m,1}^{(j-1)}) \rightarrow \mathbf{u}_{n,m,0}^{(j)} \overset{(40)}{\rightarrow} \mathbf{u}_{n,m,1}^{(j)}$$

$$\text{Step } j+1: \ U(\ldots, \mathbf{u}_{n,m,-1}, \mathbf{u}_{n,m,0}, \mathbf{u}_{n,m,1}^{(j)}) \rightarrow \mathbf{u}_{n,m,0}^{(j+1)} \overset{(40)}{\rightarrow} \mathbf{u}_{n,m,1}^{(j+1)} \tag{42}$$

$$\ldots$$

The procedure is initialized conventionally by providing an initial guess (trial solution) $\mathbf{u}_{n,m,l}^{(0)}$ for all n, m, and l. This approach is more attractive for being less involved computationally and easier to program. In some cases, though, it may lead to larger errors, since at the final step, the multiscale boundary conditions will be satisfied for the *previous* iteration only. The choice of a more adequate approach may depend on a specific problem statement, the nature of a minimization procedure utilized, and the accuracy sought. In the applications discussed below, we adopted the direct method (41) for our final calculations. However, trial usage of the iterative scheme (42) did not compromise performance of the multiscale boundary conditions noticeably.

4.2. Example 1

The first problem, depicted in Fig. 7, utilizes the multiscale boundary conditions only at the bottom layer of the fine grain domain, while fixed (zero displacement) boundary conditions are applied to the lateral faces. The atomic displacements along the deformable boundary layer $l = 1$ in the reduced domain are related with the displacements of atoms in the adjacent layer $l = 0$ through the discrete convolution operator, according to Eq. (40). The original size of the full domain is $17 \times 17 \times 50$ atomic layers, and the fine grain domain (the reduced domain) comprises 40% of the total volume, i.e., $17 \times 17 \times 20$ layers. This reduction corresponds to the value $a = 31$. According to (37), the interlayer distance along the coordinate axes is 2.066 Å, and the total height of the fine grain is 39.25 Å. The curvature radius of the indenter is 10 Å. The indentation process is simulated in a series of iteration steps, where the maximum indentation depth of 6Å is achieved at the 60th step. The interaction between indenter and substrate atoms is modeled with the Lennard Jones potential,

$$V(r) = 4\varepsilon \left(\frac{\sigma^{12}}{r^{12}} - \frac{\sigma^6}{r^6} \right), \quad \epsilon = 0.005 \text{ eV}, \quad \sigma = 2.85 \text{ Å} \tag{43}$$

where a continuous atomic density of 0.178 atom/Å^3 is assumed for the indenter (Sokolov and Henderson, 2000). We note that alternative models to characterize the tip/substrate interaction can be similarly utilized.
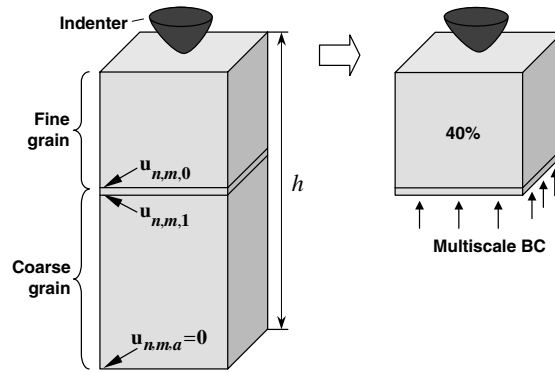
Fig. 7. Nanoindentation problem with the multiscale boundary conditions applied at the bottom face of the fine grain; h, height of the full problem.

The result of this simulation, the load/indentation depth curve, is plotted in Fig. 8 in comparison with the benchmark simulation that preserves the complete atomistic resolution for both the fine and coarse grains. The plot shows an excellent agreement between the test (full domain) and multiscale simulations at all three indentation regimes: elastic load, plasticity (the top part of the indentation curve) and unload. Meanwhile, the multiscale approach reduces the computational effort by a factor of 7.

Fig. 9 shows the structure of dislocations under the indenter tip at the indentation depth 5 Å (step 50 in Fig. 8). The dislocations were visualized using the following rule. For each specific atom, we computed the number of neighbor atoms, N_c, found within a sphere of radius $(1 + \sqrt{2})\rho/2$, where ρ is the equilibrium parameter of the potential (37). This radius is equal to the distance between the current atom and the mean point in between the first and the second neighbor shells in the present lattice structure. The coordination number $N_c = 12$ corresponds to a regular fcc structure, while another value indicates a lattice dislocation or another irregularity. The fcc dislocation cores are most often associated with $N_c = 11$ and 13; only such atoms are shown in Fig. 9. It is seen that application of the multiscale boundary conditions allows reproducing of the dislocation picture in very fine details, as compared to the benchmark simulation. At the same time, application of the standard (zero displacement) boundary conditions to the reduced domain violates the process of dislocations initiation and growth. These results indicate also that the multiscale interface should be established on a distance of about 12 {001} planes from the nearest dislocation core to assure good similarity of the results with respect to the corresponding full size problem. We note that indentation of the {001}
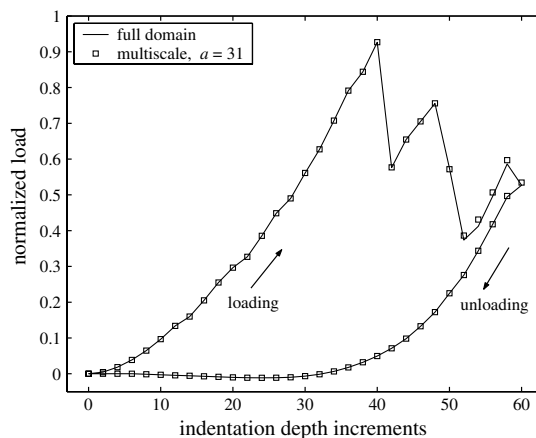

Fig. 8. Load vs. indentation depth: comparison of full domain atomistic and multiscale solutions for nanoindentation problem described in Fig. 7.
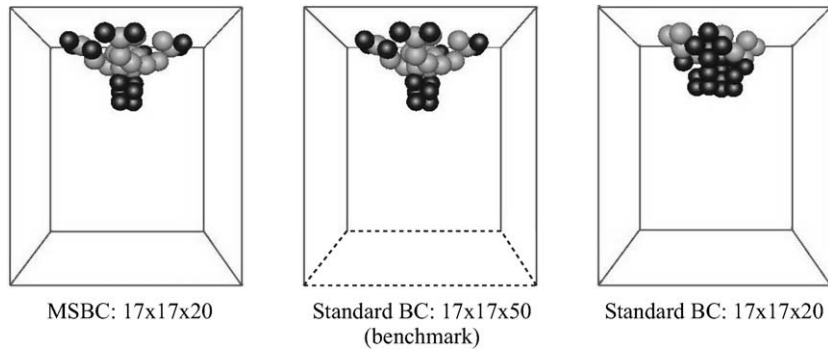
Fig. 9. Dislocation structure formed under indenter tip at step 50; comparison for the MSBC approach, and the standard lattice statics simulations for the benchmark and reduced problems. For the $17 \times 17 \times 50$ case, only the corresponding upper part of the domain is depicted. The coordination number is 11 and 13 for the light and dark grey atoms, respectively; atoms with other coordination numbers are not shown.
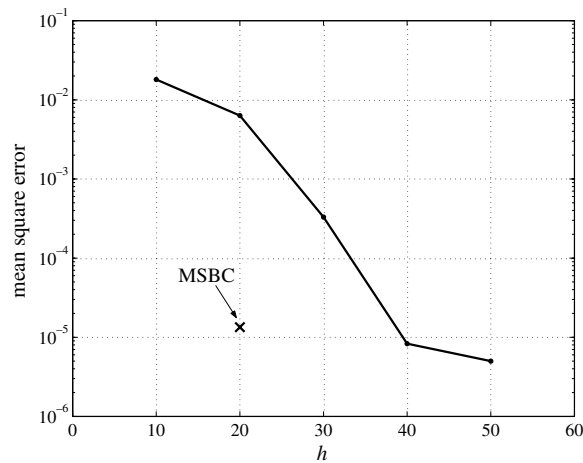

Fig. 10. Error estimate for the load/indentation depth dependence in a series of $17 \times 17 \times h$ standard full domain simulations, due to boundary effects at the bottom face of the structure. The cross indicates error for the MSBC simulation over the $17 \times 17 \times 20$ domain.

surface results in a compact stacking fault tetrahedra structure under the indenter, imposed by the compactness of the structure and the small size of the indenter. Meantime, indentation into a surface where {1 1 1} slip planes are parallel to the indentation direction may result in a long-range motion of dislocations, and therefore in a larger fine scale domain to be utilized.

The size of the benchmark problem was chosen on the basis of the following. Initially, a series of molecular mechanics simulations were accomplished over the domains $17 \times 17 \times h$ of various heights h (see Fig. 7), comprised of 10–60 layers with 10 layer increments. The standard zero displacement boundary conditions applied at the bottom and side faces of the structure. All other provisos, including the indenter size at the total indentation depth were kept invariant, identical to the above problem statement. The mean square error was evaluated for all load/indentation depth dependencies at $h < 60$ with respect to the curve corresponding to $h = 60$. The error stabilizes at $h \geqslant 40$ (see Fig. 10) and the indentation curves were found identical at $h = 50$ and 60 in all indentation regimes. Thus, the domain comprised of 50 atomic layers in height was considered as the minimal structure, required for the standard lattice statics simulations within the current problem settings.

4.3. Example 2

The second problem employs the multiscale boundary conditions separately at five planar faces of the parallelepiped fine grain, excluding the top traction free boundary, which is exposed to the indenter (see Fig. 11).
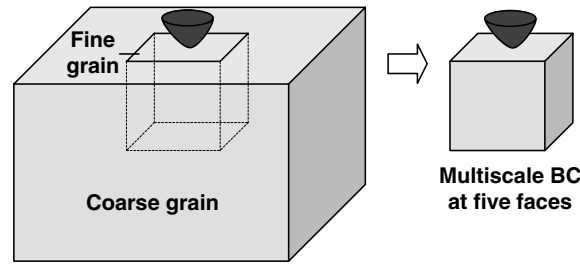
Fig. 11. Application of multiscale boundary conditions at all non-loaded faces.

All the coarse grain boundaries are fixed. Each of these plane interfaces are treated based on the lattice configuration shown in Fig. 5 and the theoretical formulation of Section 3. The relevant rotations of the coordinate system are then taken into account when implementing Eq. (40) within an appropriate molecular mechanics code.

For the current problem, the reduced domain is bounded by several intersecting interfaces of finite size, at which the multiscale boundary conditions treatment is desired, while the original 3D formulation has been obtained within assumption of an infinite interface. In treating such interfaces, the convolution sum in Eq. (40) may involve some unavailable displacements $\mathbf{u}_{n,m,0}^{(\mathrm{na})}$. These unavailable displacements correspond to lattice sites that lie outside the actual physical domain utilized for the multiscale simulation. Thus, one possibility is to assume that all

$$\mathbf{u}^{(\mathrm{na})} = \mathbf{0} \tag{44}$$

However, this would create a sharp gradient in the displacement field at the MD boundary; to preserve smoothness and entirely consistent with the approximation of linearity of displacement at the boundary, we enforce that

$$\mathbf{u}^{(\mathrm{na})} = \mathbf{u}^{(\mathrm{edge})} \tag{45}$$

where $\mathbf{u}^{(\mathrm{edge})}$ represent displacements on the edge of the simulated domain in the closest vicinity of an unavailable atom $(n,m,0)$.

For a small interface, where the number of atoms along one of the edges is comparable with the values of parameters n_c and m_c in Eq. (40), the assumption (44) or (45) may result in some errors, which we refer to as the "corner effect" in 2D, or "edge effect" in 3D simulations. Besides, undue smallness of the fine grain may constrain the processes of plastic deformation. The positive side of this issue is the following: with an increase of the fine scale domain, the number of "problematic" nodes that may impose the edge effect in 3D applications increases linearly—proportionally to the linear dimension of the domain, while the number of "good" nodes increases quadratically—proportionally to the surface area of the multiscale interface. Thus, for each specific lattice and loading conditions, there should exist some minimal size of the fine grain, such that for any larger domain this effect is negligible. The purpose of the present analysis is to find out the smallest lateral size of the fcc interface, such that simulation results are not affected by the edge effect. We will vary the fine grain dimensions, as well as the size of the coarse scale domain, determined by the parameter a, while all other provisos will be kept constant. The results will be compared with the benchmark molecular mechanics solutions accomplished over the full original domain.

We have considered separately two fine grain sizes, $24 \times 24 \times 24$ and $48 \times 48 \times 48$ lattice sites, and for each of these sizes we utilized two values of the coarse scale parameter, $a = 7$ and 13. All other conditions are identical for these problems: the indentation is accomplished in a series of iteration steps, where the maximum indentation depth of 8.8 Å is achieved at the 44th step; indenter radius and other provisos are similar to the Example 1.

The results of the multiscale and benchmark full domain simulations are compared in Fig. 12. It is seen that the use of a larger fine grain leads to a better agreement with the benchmark solutions, particularly during the plastic deformation phase. For the smaller fine grain, the performance is worse compared to Example 1
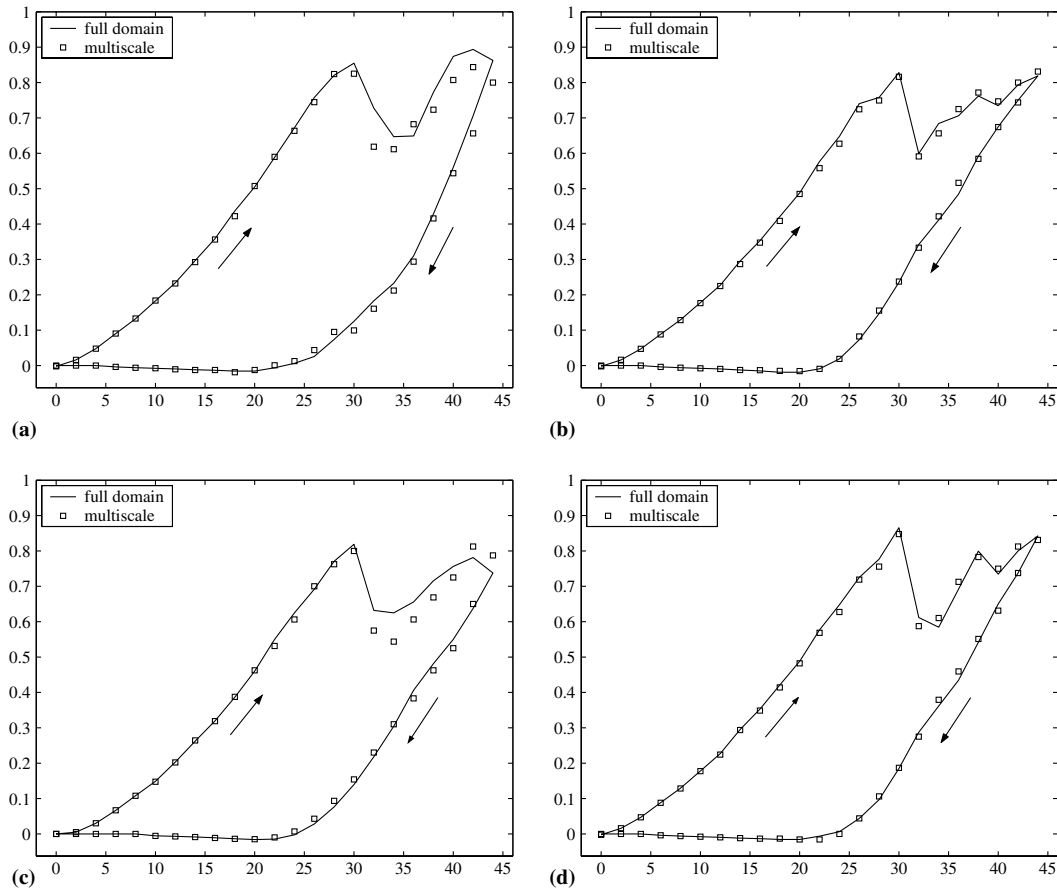
Fig. 12. Normalized load (vertical axes) vs. indentation depth increments (horizontal axes) for the second problem, Fig. 11. Results are given for various fine grain sizes and coarse scale parameters. (a) $24 \times 24 \times 24$, $a = 7$; (b) $48 \times 48 \times 48$, $a = 7$; (c) $24 \times 24 \times 24$, $a = 13$; (d) $48 \times 48 \times 48$, $a = 13$.

(Fig. 8), which utilizes even smaller fine scale domain at comparable loading conditions. Therefore, we attribute the discrepancy between the multiscale and benchmark results in the present problem to the corner effect only. This leads to a conclusion that the minimal effective dimension of the fcc interface allowing to diminish the corner effect is about 50 interplanar distances in the direction [1 0 0], [0 1 0] or [0 0 1]. The second trend observed by comparing the results at a constant fine grain size is the invariance of the performance as depending on the value a. In other words, the coarse grain size can be fairly arbitrary, once a sufficiently large fine grain is chosen. Stable convergence is also observed for the elastic loading and unloading phases, which represent bulk materials properties in experimental indentation measurements. We finally note that better performance observed in Example 1 for a smaller domain is due to the fixed boundary conditions utilized for the side faces of the full and fine grain domains. These boundary conditions provide similar constraints for the deformation and plasticity in both benchmark and multiscale simulations of this problem; besides, the issue of corner effects does not arise for a *single* multiscale interface utilized in Example 1.

5. Conclusion

In this paper, we have presented the multiscale boundary conditions for quasistatic atomistic simulations in crystalline solids. Homogeneous character of the coarse grain material deformation results in small relative displacements of atoms at the boundary of the crystalline structure. This allows the present multiscale approach, which does not involve a continuum averaging and a consequent coupling of the atomistic and

continuum models. As a result, the method does not involve an artificial handshake region. It utilizes spatial regularity of crystalline solids, and enables one to calculate the quasistatic response of the coarse grain, the peripheral elastic domain, on the intrinsic atomic level. The lattice translation symmetry along the fine/coarse grain interface is employed by means of the discrete Fourier transform to yield a compact formulation in terms of a discrete convolution operator. This operator represents the response behavior of the coarse grain, and provides boundary conditions for the atomistic simulation over a localized domain of interest. As a result, the computer simulations can be run for the localized atomistic domain only, while all the coarse grain degrees of freedom are eliminated. This gives a possibility for drastic savings in computational time—up to several orders of the magnitude. The method is most adequate in applications to problems with simple coarse grain geometries, where the peripheral boundaries follow a planar setup, similar to one chosen for the multiscale interface, i.e., for the boundary of the local region of interest. In problems with complex coarse scale geometries and force distributions, the available hybrid multiscale techniques can be more versatile. The major advantages of the present approach in comparison with the hybrid techniques are the simplicity of the final working formulation, Eq. (18) or (34), and the straightforward implementation for a readily available molecular mechanics energy minimization code.

This method has been verified in a series of nanoindentation simulations. The multiscale boundary conditions according to (40) have been shown to perform well for a wide range of indentation depths and method parameters, where a good agreement with the benchmark full domain solution was observed. All three regimes, elastic load, plastic deformation of the substrate around the indenter tip, and unload were reproduced adequately. Plastic behavior is implied by bond breaking processes within the fine grain domain, and it is represented by the discontinuous character at a later phase of the loading process. The non-linear/plastic behavior is allowed inside the simulated domain, because the formulation assumes linearity only in the vicinity of the interface between the atomistic and peripheral elastic domains. Regarding the performance of the method, there are two general guidelines that can enable the practitioner to determine an adequate, yet computationally effective fine/coarse grain partitioning: (1) performance of the multiscale boundary conditions improves with the increase of a fine grain, and (2) performance is typically invariant with respect to the size of a coarse grain. In other words, once a sufficiently large fine grain is chosen, linear dimensions of the coarse grain can be fairly arbitrary. Applicability conditions, which guarantee good performance of this method, can be summarized as the following: (1) the coarse grain and the fine/coarse grain interface are dislocation-free, and their deformation is linear elastic (in the hypothetical fully atomistic model); (2) linear dimension of the fine grain in the corresponding lattice direction is larger than the length occupied 50 unit cells. The second of these conditions has to be satisfied in order to eliminate corner effects in applications to two- and three-dimensional structures.

Properties of the kernel matrices of the interface operator have been investigated on an fcc gold lattice with a pair-wise potential. Components of these matrices appear to decay quickly with the growth of spatial order parameters; this allows truncating the corresponding convolution summations and leads to the numerical efficiency of this method. Another interesting property of the kernel matrices is their invariance with respect to the choice of the interatomic potential, so that it serves as a fundamental characteristic of the fcc geometry with the nearest neighbor interaction. Furthermore, a general systematic analysis of the asymptotic and invariant properties of the multiscale operators is an objective for future.

A fully self-consistent dynamic formulation of this method, involving also recognition of dislocation patterns and their passage to the coarse grain, is also a future challenge. Similar to other multiscale approaches, the current method requires a priori knowledge of the non-linear plastic zone; exclusions are the QC method, e.g., Ortiz et al. (2001), and the method by Shilkrot et al. (2004). However, localized inhomogeneities, such as the lattice dislocations, can be arranged to pass the multiscale interface and absorbed by the coarse scale region within a straightforward extension, which will be discussed in a future publication. The basic idea will consist in early identification of a dislocation in a release zone within the fine grain, and redefining the fine/coarse interface after the dislocation is transferred through the interface. The authors are also working on applications of the present methodology to periodic nanostructures, such as carbon nanotubes, nanowires and graphene monolayers, e.g. Medyanik et al. (2005). A broader task for the future consists in creation of a database of the kernel matrices corresponding to major Bravais lattices governed by popular interatomic

potentials, including the many-body potentials. This database, once available, could serve as a valuable resource for extensive usage by the computational mechanics community.

Appendix A

A.1. Discrete Fourier transform

The inversion formula (8) for a finite sequence can be derived on the basis of the following. First note that any finite sequence $\{g_n\}$ at $n \in [n_{\min}, n_{\max}]$, can be considered formally as an infinite sequence at $n \in [-\infty, \infty]$ with all zero elements in the range $n < n_{\min}$ and $n > n_{\max}$. Most generally, the inverse DFT of such a sequence can be evaluated as an integral of the 2π-periodic function (7),

$$g_n = \frac{1}{2\pi} \int_{-\pi}^{\pi} \hat{g}(p) e^{ipn} \, \mathrm{d}p \tag{A.1}$$

Indeed, employ the DFT in the form (7) for the above integral and rearrange it to get

$$\frac{1}{2\pi} \int_{-\pi}^{\pi} \sum_{n'} g_{n'} e^{-ipn'} e^{ipn} \, \mathrm{d}p = \frac{1}{2\pi} \sum_{n'} g_{n'} \int_{-\pi}^{\pi} e^{-ip(n'-n)} \, \mathrm{d}p = \sum_{n'} g_{n'} \delta_{n,n'} = g_n \tag{A.2}$$

Here, δ is the Kronecker delta; n and n' are integers.

The integral (A.1) can be approximated by applying the midpoint integration rule,

$$\int_a^b f(x) \, \mathrm{d}x \approx h \left[f\left(\frac{x_0 + x_1}{2}\right) \cdots + f\left(\frac{x_{J-1} + x_J}{2}\right) \right], \quad h = \frac{b-a}{J}, \;\; x_k = a + hk \tag{A.3}$$

If the wave number p is discretized as

$$p = \frac{\pi v_p}{N}, \quad v_p = \pm\frac{1}{2}, \pm\frac{3}{2}, \ldots, \pm N \mp \frac{1}{2} \tag{A.4}$$

then application of the midpoint rule to (A.1) yields

$$g_n \approx \frac{1}{2N} \sum_{v_p = 1/2 - N}^{N - 1/2} \hat{g}\left(\frac{\pi v_p}{N}\right) e^{i\pi v_p n / N} \tag{A.5}$$

The value $2N$ must correspond to the range of non-trivial elements in the original real space sequence $\{g_n\}$, i.e., $2N = n_{\max} - n_{\min} + 1$.

The nature of Fourier integrals is such that discretization procedures of the type (A.4) and (A.5) yield the *exact* real space sequences. Indeed,

$$\frac{1}{2N} \sum_{v_p = 1/2 - N}^{N - 1/2} \hat{g}\left(\frac{\pi v_p}{N}\right) e^{i\pi v_p n / N} = \frac{1}{2N} \sum_{v_p = 1/2 - N}^{N - 1/2} \left(\sum_{n'} g_{n'} e^{-i\pi v_p n' / N} \right) e^{i\pi v_p n / N}$$

$$= \frac{1}{2N} \sum_{n'} g_{n'} \sum_{v_p = 1/2 - N}^{N - 1/2} e^{-i\pi v_p n' / N} e^{i\pi v_p n / N} = \sum_{n'} g_{n'} \delta_{n,n'} = g_n \tag{A.6}$$

Thus, we can employ an equality sign in (A.5) and obtain the inversion formula (8).

The *convolution theorem* (9) can be proved as the following:

$$\mathscr{F}\left\{\sum_{n'} f_{n-n'} g_{n'}\right\} = \sum_{n}\sum_{n'} f_{n-n'} g_{n'} e^{-ipn} = \sum_{n}\sum_{n'} f_{n-n'} g_{n'} e^{-ip(n-n')} e^{-ipn'}$$

$$= \sum_{n'}\sum_{n} f_{n-n'} e^{-ip(n-n')} g_{n'} e^{-ipn'} = \sum_{n'} \hat{f}(p) g_{n'} e^{-ipn'} = \hat{f}(p)\hat{g}(p) \tag{A.7}$$

Note that the range of summations in the above relationships is, in principle, from $-\infty$ to ∞.

The *shift theorem* (10) is proved by utilizing a similar procedure

$$\mathscr{F}\{g_{n+h}\} = \sum_{n} g_{n+h} e^{-ipn} = \sum_{n} g_{n+h} e^{-ip(n+h)} e^{iph} = \hat{g}(p) e^{iph} \tag{A.8}$$

where value h is integer.

A.2. Derivation of K-matrices

There exist two approaches to practical implementation of the symbolic expression (25). The first of these is a *numerical* approach consisting in the following. Consider a numerical model of the regular fcc structure, where all atoms are rigidly fixed at the equilibrium positions; for a lattice governed by (37), these positions are determined by the radius vectors

$$\mathbf{r}_{n,m,l}^{\text{eq}} = \frac{\rho}{\sqrt{2}}\begin{pmatrix} n \\ m \\ l \end{pmatrix}, \quad n+m+l - \text{even} \tag{A.9}$$

where n, m and l is the atomic numbering shown in Fig. 5. The frame origin is associated with the atom $(0,0,0)$ (see Fig. A.1). Within the nearest neighbor interaction assumption, atoms associated with the vectors (A.9) also serve as the lattice unit cells. The numerical model must include the cell at origin and all the adjacent cells interacting directly with it. Thus, we construct a numerical model for the atom $(0,0,0)$ and its 12 closest neighbors of the type shown in Fig. A.1.

On the next stage we perturb the equilibrium position of the origin atom $(0,0,0)$ along the *x*-axis by a small value $\delta x_{0,0,0} \ll \rho$, while all other atoms are kept fixed at the initial positions (A.9). Then we measure (i.e., evaluate numerically) three components of the force exerted on the atom at origin due such a perturbation: f^x, f^y and f^z. The ratios of these forces with respect to the value of displacement $\delta x_{0,0,0}$ comprise the first column of the matrix $\mathbf{K}_{0,0,0}$. This procedure is repeated by perturbing the *y*- and *z*-axis positions of the origin atom at $\delta y_{0,0,0} \ll \rho$ and $\delta z_{0,0,0} \ll \rho$, accordingly, in order to obtain two remaining columns of the matrix $\mathbf{K}_{0,0,0}$. The position perturbation procedure is repeated also for the 12 neighboring atoms, while the force components
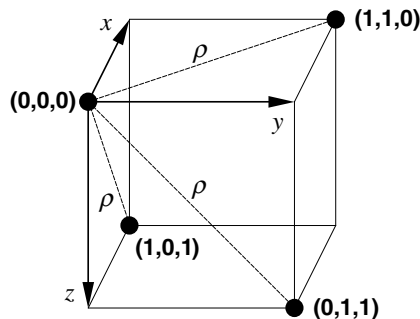

Fig. A.1. Three nearest neighbors for the current atom $(0,0,0)$ in the fcc structure. There are in total 12 such neighbors for each specific lattice atom; for the atom at origin, these are $(\pm1,\pm1,0)$, $(\pm1,0,\pm1)$, $(0,\pm1,\pm1)$, $(\pm1,\mp1,0)$, $(\pm1,0,\mp1)$ and $(0,\pm1,\mp1)$. The neighbors are found at the equilibrium distance ρ, which is considered as a parameter of the interatomic potential (37).

f^x, f^y and f^z are still measured at the origin atom. For each specific neighbor atom (n, m, l), one additional matrix $\mathbf{K}_{-n,-m,-l}$ is assembled. In general, the above procedure can be expressed by the following:

$$\mathbf{K}_{-n,-m,-l} \approx \begin{pmatrix} \dfrac{f^x}{\delta x_{n,m,l}} & \dfrac{f^x}{\delta y_{n,m,l}} & \dfrac{f^x}{\delta z_{n,m,l}} \\[2mm] \dfrac{f^y}{\delta x_{n,m,l}} & \dfrac{f^y}{\delta y_{n,m,l}} & \dfrac{f^y}{\delta z_{n,m,l}} \\[2mm] \dfrac{f^z}{\delta x_{n,m,l}} & \dfrac{f^z}{\delta y_{n,m,l}} & \dfrac{f^z}{\delta z_{n,m,l}} \end{pmatrix}, \quad n + m + l - \text{even} \tag{A.10}$$

Matrices for odd $n + m + l$ are regarded to be trivial.

For relatively simple potentials of interaction, one may also exercise the following *analytical* approach to the derivation of K-matrices. This approach is exact, though it may appear intractable for complex long-ranged potentials. In below we discuss this technique in application to the present fcc model. Consider the lattice potential energy associated with the interaction of the current atom $(0, 0, 0)$ with its neighbors within the range of the interatomic potential. This energy is given 12 pair-wise terms in the form

$$U = V(|\mathbf{r}_{1,1,0} - \mathbf{r}_{0,0,0}|) + V(|\mathbf{r}_{1,0,1} - \mathbf{r}_{0,0,0}|) + \underset{10 \text{ analogous terms}}{\dots} \tag{A.11}$$

where V is the Morse potential (25). The variable vectors $\mathbf{r}_{n,m,l}$ describe current positions of atoms (n, m, l) in a deformed lattice. These vectors can be replaced by the sums,

$$\mathbf{r}_{n,m,l} = \mathbf{r}_{n,m,l}^{\text{eq}} + \mathbf{u}_{n,m,l} \tag{A.12}$$

where $\mathbf{r}_{n,m,l}^{\text{eq}}$ is the constant vector (A.9), and $\mathbf{u}_{n,m,l} = (u_{n,m,l}^x, u_{n,m,l}^y, u_{n,m,l}^z)$ is the variable vector of displacements of the atom (n, m, l). Then the arguments of function V in Eq. (A.11) can be rewritten as

$$|\mathbf{r}_{n,m,l} - \mathbf{r}_{0,0,0}| = |\mathbf{r}_{n,m,l}^{\text{eq}} + \mathbf{u}_{n,m,l} - \mathbf{r}_{0,0,0}^{\text{eq}} - \mathbf{u}_{0,0,0}|$$

$$= \left[\left(\frac{n\rho}{\sqrt{2}} + u_{n,m,l}^x - u_{0,0,0}^x \right)^2 + \left(\frac{m\rho}{\sqrt{2}} + u_{n,m,l}^y - u_{0,0,0}^y \right)^2 + \left(\frac{l\rho}{\sqrt{2}} + u_{n,m,l}^z - u_{0,0,0}^z \right)^2 \right]^{\frac{1}{2}} \tag{A.13}$$

Substitution of these arguments into (A.11), provides the potential energy in terms of the atomic displacements, i.e., $U(\mathbf{u})$ symbolically. Finally, the K-matrices are derived by evaluating the second derivatives (25) in closed form,

$$\mathbf{K}_{-n,-m,-l} = \mathbf{K}_{n,m,l} = - \begin{pmatrix} \dfrac{\partial^2 U(\mathbf{u})}{\partial u_{0,0,0}^x \, \partial u_{n,m,l}^x} & \dfrac{\partial^2 U(\mathbf{u})}{\partial u_{0,0,0}^x \, \partial u_{n,m,l}^y} & \dfrac{\partial^2 U(\mathbf{u})}{\partial u_{0,0,0}^x \, \partial u_{n,m,l}^z} \\[3mm] \dfrac{\partial^2 U(\mathbf{u})}{\partial u_{0,0,0}^y \, \partial u_{n,m,l}^x} & \dfrac{\partial^2 U(\mathbf{u})}{\partial u_{0,0,0}^y \, \partial u_{n,m,l}^y} & \dfrac{\partial^2 U(\mathbf{u})}{\partial u_{0,0,0}^y \, \partial u_{n,m,l}^z} \\[3mm] \dfrac{\partial^2 U(\mathbf{u})}{\partial u_{0,0,0}^z \, \partial u_{n,m,l}^x} & \dfrac{\partial^2 U(\mathbf{u})}{\partial u_{0,0,0}^z \, \partial u_{n,m,l}^y} & \dfrac{\partial^2 U(\mathbf{u})}{\partial u_{0,0,0}^z \, \partial u_{n,m,l}^z} \end{pmatrix}_{\mathbf{u}=0} \tag{A.14}$$

followed by replacing the displacement components, $u_{n,m,l}^x$, $u_{n,m,l}^y$ and $u_{n,m,l}^z$, with zeros at all n, m and l. The later procedure is symbolized by the subscript notation $\mathbf{u} = 0$. Derivation of the closed form derivatives for (A.14) is convenient by utilizing symbolic tools of Maple or Mathematica software packages.

References

Abraham, F.F., Broughton, J.Q., Bernstein, N., Kaxiras, E., 1998. Spanning the continuum to quantum length scales in a dynamic simulation of brittle fracture. Europhysics Letters 44 (6), 783–787.

Broughton, J.Q., Abraham, F.F., Bernstein, N., Kaxiras, E., 1999. Concurrent coupling of length scales: methodology and application. Physical Review B 60 (4), 2391–2403.

Curtin, W.A., Miller, R.E., 2003. Atomistic/continuum coupling in computational materials science. Modelling and Simulation in Materials Science and Engineering 11, R33–R68.

Deymier, P.A., Vasseur, J.O., 2002. Concurrent multiscale model of an atomic crystal coupled with elastic continua. Physical Review B 66 (13), 134106.

Harrison, D.E., 1988. Application of molecular dynamics simulations to the study of ion-bombarded metal surfaces. Critical Reviews in Solid State and Materials Science 14 (Sup.1), S1–S78.

Karpov, E.G., Stephen, N.G., Dorofeev, D.L., 2002. On static analysis of finite repetitive structures by discrete Fourier transform. International Journal of Solids and Structures 39 (16), 4291–4310.

Karpov, E.G., Stephen, N.G., Liu, W.K., 2003. Initial tension in randomly disordered periodic lattices. International Journal of Solids and Structures 40 (20), 5371–5388.

Karpov, E.G., Wagner, G.J., Liu, W.K., 2005. A Green's function approach to deriving wave-transmitting boundary conditions in molecular dynamics simulations. International Journal for Numerical Methods in Engineering 62 (9), 1250–1262.

Liu, W.K., Karpov, E.G., Zhang, S., Park, H.S., 2004. An introduction to computational nano mechanics and materials. Computer Methods in Applied Mechanics and Engineering 193 (17–20), 1529–1578.

Medyanik, S.A., Karpov, E.G., Liu, W.K., 2005. Domain reduction method for atomistic simulations. Journal of Computational Physics, submitted for publication.

Ortiz, M., Cuitino, A.M., Knap, J., Koslowski, M., 2001. Mixed atomistic continuum models of material behavior: the art of transcending atomistics and informing continua. MRS Bulletin 26 (3), 216–221.

Park, H.S., Karpov, E.G., Liu, W.K., 2005a. Non-reflecting boundary conditions for atomistic, continuum and coupled atomistic/continuum simulations. International Journal for Numerical Methods in Engineering 64, 237–259.

Park, H.S., Karpov, E.G., Liu, W.K., Klein, P.A., 2005b. The bridging scale for two-dimensional atomistic/continuum coupling. Philosophical Magazine 85 (1), 79–113.

Park, H.S., Karpov, E.G., Klein, P.A., Liu, W.K., 2005c. Three-dimensional bridging scale analysis of dynamic fracture. Journal of Computational Physics 207, 588–609.

Rudd, R.E., Broughton, J.Q., 1998. Coarse-grained molecular dynamics and the atomic limit of finite elements. Physical Review B 58 (10), R5893–R5896.

Rudd, R.E., Broughton, J.Q., 2000. Concurrent coupling of length scales in solid state systems. Physica Status Solidi B 217 (1), 251–291.

Ryvkin, M., Fuchs, M.B., Nuller, B., 1999. Optimal design of infinite repetitive structures. Structural Optimization 18 (2–3), 202–209.

Shenoy, V.B., Miller, R., Tadmor, E.B., Phillips, R., Ortiz, M., 1998. Quasicontinuum models of interfacial structure and deformation. Physical Review Letters 80 (4), 742–745.

Shilkrot, L.E., Miller, R.E., Curtin, W.A., 2004. Multiscale plasticity modeling: coupled atomistics and discrete dislocation mechanics. Journal of the Mechanics and Physics of Solids 52 (4), 755–787.

Sokolov, I.Y., Henderson, G.S., 2000. The height dependence of image contrast when imaging by non-contact afm. Surface Science 464 (2–3), L745–L751.

Tadmor, E.B., Phillips, R., Ortiz, M., 1996. Mixed atomistic and continuum models of deformation in solids. Langmuir 12 (19), 4529–4534.

Wagner, G.J., Liu, W.K., 2003. Coupling of atomistic and continuum simulations using a bridging scale decomposition. Journal of Computational Physics 190, 249–274.

Wagner, G.J., Karpov, E.G., Liu, W.K., 2004. Molecular dynamics boundary conditions for regular crystal lattices. Computer Methods in Applied Mechanics and Engineering 193 (17–20), 1579–1601.